

Clustering, Cosmology and a New Era of Black Hole Demographics – I. The Conditional Luminosity Function of Active Galactic Nuclei

D. R. Ballantyne^{*}

Center for Relativistic Astrophysics, School of Physics, Georgia Institute of Technology, 837 State Street, Atlanta, GA 30332-0430, USA

Accepted XXX. Received YYY; in original form ZZZ

ABSTRACT

Deep X-ray surveys have provided a comprehensive and largely unbiased view of active galactic nuclei (AGN) evolution stretching back to $z \sim 5$. However, it has been challenging to use the survey results to connect this evolution to the cosmological environment that AGNs inhabit. Exploring this connection will be crucial to understanding the triggering mechanisms of AGNs and how these processes manifest in observations at all wavelengths. In anticipation of upcoming wide-field X-ray surveys that will allow quantitative analysis of AGN environments, this paper presents a method to observationally constrain the Conditional Luminosity Function (CLF) of AGNs at a specific z . Once measured, the CLF allows the calculation of the AGN bias, mean dark matter halo mass, AGN lifetime, halo occupation number, and AGN correlation function – all as a function of luminosity. The CLF can be constrained using a measurement of the X-ray luminosity function and the correlation length at different luminosities. The method is illustrated at $z \approx 0$ and 0.9 using the limited data that is currently available, and a clear luminosity dependence in the AGN bias and mean halo mass is predicted at both z , supporting the idea that there are at least two different modes of AGN triggering. In addition, the CLF predicts that $z \approx 0.9$ quasars may be commonly hosted by haloes with $M_h \sim 10^{14} M_\odot$. These ‘young cluster’ environments may provide the necessary interactions between gas-rich galaxies to fuel luminous accretion. The results derived from this method will be useful to populate AGNs of different luminosities in cosmological simulations.

Key words: galaxies: active – galaxies: haloes – quasars: general – galaxies: Seyfert – X-rays: galaxies – dark matter

1 INTRODUCTION

The supermassive black holes that lurk at the center of almost all massive galaxies play an important, but still largely mysterious, role in the formation and evolution of their host galaxies. Significant amounts of energy and momentum can be deposited in the central regions of a galaxy when the black hole is accreting rapidly from its surroundings and shining as an active galactic nucleus (AGN; Hopkins et al. 2005; Springel, Di Matteo & Hernquist 2005). The AGN phase of a galaxy may therefore exert a significant influence on the overall size and evolution of the galaxy (e.g., Di Matteo et al. 2005; Croton et al. 2006; Menci et al. 2006; Hopkins et al. 2008). Unraveling the physics behind the triggering of AGN activity and its influence on the host galaxy

is an important ingredient for a complete picture of galaxy formation and evolution.

As the AGN phase is crucial to galaxy evolution, there has been tremendous interest in determining a comprehensive census of AGN activity in the Universe, and how it changes over cosmic time (e.g., Brandt & Hasinger 2005; Triester & Urry 2012; Merloni & Heniz 2013; Brandt & Alexander 2015). This demography of accreting black hole has its roots in the optical quasar surveys of the 1980s (e.g., Hartwick & Schade 1990), but it is now understood that deep X-ray surveys provide the least biased determination of AGN activity in the Universe (e.g., Brandt & Alexander 2015). As a result, the last decade has witnessed an army of X-ray telescopes perform numerous extragalactic surveys that, when combined,

^{*} E-mail: david.ballantyne@physics.gatech.edu

are painting a clear and consistent picture of AGN¹ activity up to $z \sim 5$ (e.g., Ueda et al. 2003; La Franca et al. 2005; Ueda et al. 2014; Aird et al. 2010, 2015a,b; Buchner et al. 2015; Georgakakis et al. 2015). Analysis of the resulting X-ray luminosity functions (XLFs) show that AGNs underwent strong luminosity and density evolution with time, so that the luminosity corresponding to the peak density drops at lower z (e.g., Ueda et al. 2014; Aird et al. 2015a). This evolution is likely associated with changes in the AGN fueling and triggering physics as the Universe expanded (e.g., Georgakakis et al. 2009; Hickox et al. 2009; Allevato et al. 2011; Draper & Ballantyne 2012; Hopkins et al. 2014).

A limitation of many of the existing deep X-ray surveys is their narrow field of view, which limits the investigation of how AGNs are connected to their cosmological environment. This problem becomes especially acute as one of the leading models of AGN triggering is mergers and interactions between galaxies (e.g., Sanders et al. 1988; Hernquist 1989; Kauffmann & Haehnelt 2000; Di Matteo et al. 2005; Hopkins et al. 2005, 2006, 2008). Moreover, numerical simulations of galaxy and black hole evolution in cosmological volumes require rigorous, quantitative constraints on not just the numbers and luminosities of AGNs at a specific redshift, but also on how they are distributed throughout the galaxy population. This information can be provided by measuring the clustering of AGN as a function of luminosity and redshift, but the wide-area surveys needed for precise measurements are generally not available in the X-ray band (Cappelluti et al. 2012). The clustering of optical quasars has been explored for several years (e.g., Porciani et al. 2004; Croom et al. 2005; Myers et al. 2007; Ross et al. 2009; Zehavi et al. 2011; Shen et al. 2013; Eftekharzadeh et al. 2015), but is not able to provide an unbiased sample of black hole activity (e.g., Mendez et al. 2016).

This observational landscape will be changing, however, as both *eROSITA* and *Athena* will be performing wide-field X-ray surveys that will allow precise AGN clustering measurements at these energies (Kolodzig et al. 2013a,b). The addition of clustering data to the traditional suite of AGN demographic information (luminosity function, obscuration fraction, etc.) will provide a powerful tool to understanding how AGNs of different luminosities connect to their large scale environments. This paper and its companion (hereafter, Paper II; Ballantyne 2016) presents a theoretical framework, and some initial results, of how one might exploit the potential in the new era of AGN demographics. The underlying concept presented here is the *conditional luminosity function* (CLF), first developed for galaxy clustering studies by Yang et al. (2003) and van den Bosch et al. (2003). The CLF is a statistical connection between the AGN luminosity function and cosmological structure that underpins the clustering data. Constraining the CLF allows one to perform calculations in both the traditional AGN demographics 'space' (i.e., number counts, X-ray background spectra) and the clustering/dark-matter 'space' (i.e., bias, mean halo mass). This framework should also provide a method for

comparing observational data from the new wide-field X-ray surveys to predictions of cosmological galaxy evolution simulations.

This paper provides the basic description of the CLF framework for the application of X-ray surveys of AGNs (Section 2), and then applies this analysis to AGNs at $z \approx 0$ and $z \approx 0.9$ (Section 3) using the limited existing X-ray survey data with results presented in Section 4. The implications of these results for models and AGN triggering and evolution are discussed in Section 5, while general conclusions are summarized in the final Section. The Appendices collect several details of the calculation procedures, as well as other supplemental results that may be of more specialized use. Paper II shows how to apply this CLF framework to subsets of AGNs, in particular obscured and unobscured AGNs at $z \approx 0$ and 0.9. A WMAP9 Λ CDM cosmology is assumed for both papers: $h = 0.7$, $\Omega_m = 0.279$, $\Omega_\Lambda = 0.721$ and $\sigma_8 = 0.821$ (Hinshaw et al. 2013).

2 THE CONDITIONAL LUMINOSITY FUNCTION OF AGNS

This section presents an overview of the CLF and how it provides a powerful tool to connect the evolution of AGNs to their cosmological surroundings. Much of the mathematical description of the CLF shown below was presented earlier in the context of galaxy clustering (Yang et al. 2003; van den Bosch et al. 2003, 2007), but is repeated here for completeness. Finally, the CLF framework falls under the more general description of a Halo Occupation Distribution (HOD) model of clustering. HOD modeling of AGN clustering has begun to be more common in the last several years (Miyaji et al. 2011; Richardson et al. 2012, 2013; Shen et al. 2013), but much of the work necessarily focuses on luminosity-integrated quantities. As is seen below, the luminosity-dependent CLF will be particularly important for AGN clustering measurements expected in the near future.

2.1 Definitions and Useful Formulas

We define the CLF of a specific sample of AGNs, $\Psi(L|M_h)$, so that

$$\phi(L) = \int_0^\infty \Psi(L|M_h) n(M_h) dM_h, \quad (1)$$

where $\phi(L) = d\Phi(L)/d(\log L)$ is the XLF in the 2–10 keV energy band and $n(M_h)$ is the dark matter halo mass function. All of these quantities are evaluated at a specific redshift z , but the z -dependence is omitted for clarity. It is important to emphasize that $\Psi(L|M_h)$ is really a statistical description of how AGNs are distributed in haloes, where $\Psi(L|M_h)dL$ is the mean number of AGNs in a halo of mass M_h with a 2–10 keV luminosity L in the interval $L \pm dL/2$. As such, it is not a physical quantity in the sense that its functional form can be calculated from first principles. However, given the appropriate datasets, the form of $\Psi(L|M_h)$ can be constrained, and then used to compute statistics of interesting physical properties of the specified AGN population. For example, the mean number of AGNs in a luminosity interval

¹ At least for Compton-thin AGNs. Accreting black holes that are absorbed by Compton-thick material are difficult to detect outside of the local Universe (Brandt & Hasinger 2005), so their contribution and evolution remains largely unknown.

$[L_1, L_2]$ as a function of M_h is

$$\langle N(M_h) \rangle = \int_{L_1}^{L_2} \Psi(L|M_h) dL, \quad (2)$$

and then the average M_h hosting an AGN with a luminosity in this interval is (Yang et al. 2003)

$$\begin{aligned} \langle M_h(L) \rangle &= \frac{\int_0^\infty M_h \langle N(M_h) \rangle n(M_h) dM_h}{\int_0^\infty \langle N(M_h) \rangle n(M_h) dM_h} \\ &= \frac{1}{\phi(L)} \int_0^\infty M_h \langle N(M_h) \rangle n(M_h) dM_h. \end{aligned} \quad (3)$$

Tracking these quantities as a function of z will provide important insights into how AGNs evolve and their dependence on their environment.

The CLF also allows a direct estimate of the AGN lifetime or duty cycle as a function of luminosity. Martini & Weinberg (2001) showed that an estimate of the AGN lifetime would be

$$\tau_{\text{AGN}}(L) = \frac{v_{\text{AGN}}(L, M_h)}{v(M_h)} \tau_{\text{Hubble}}, \quad (4)$$

where $v_{\text{AGN}}(L, M_h)$ is the space density of AGNs with luminosity L present in haloes with mass M_h , $v(M_h) = n(M_h) dM_h$ is the space density of those haloes, and τ_{Hubble} is the Hubble time at the z of interest. Using the CLF of AGNs, the numerator can be replaced with $\Psi(L|M_h) n_h dL dM_h$, and, after replacing the halo mass with $\langle M_h(L) \rangle$, $\tau_{\text{AGN}}(L)$ can be simply written as

$$\tau_{\text{AGN}}(L) = (\Psi(L|\langle M_h(L) \rangle)) dL \tau_{\text{Hubble}}. \quad (5)$$

2.2 How To Determine the AGN CLF

As the CLF is purely a statistical description of the AGN population, it has to be constrained from measurements. The first important dataset is the XLF (i.e., the left-hand side of Eq. 1), but this is not enough on its own, as even after specifying the halo mass function $n(M_h)$, there is an infinite number of possible $\Psi(L|M_h)$ that can result in the measured XLF. Thus, additional information that depends on both luminosity and halo mass is required to determine the shape of the CLF. As shown by Yang et al. (2003) and van den Bosch et al. (2003) for galaxies, the variation of correlation lengths with luminosity, $r_0(L)$, can provide the needed measurements.

The correlation lengths come from measurements of the AGN two-point correlation function $\xi_{\text{AA}}(r)$ which measures the probability above random chance that two random AGNs within a volume element dV will be separated by a physical distance r :

$$dP = v[1 + \xi_{\text{AA}}(r)] dV, \quad (6)$$

where v is the mean number density of AGNs in dV (Peebles 1980). Observations of $\xi_{\text{AA}}(r)$ at both the optical and X-ray wavelengths show that $\xi_{\text{AA}}(r)$ is well approximated by a power-law, $\xi_{\text{AA}} = (r/r_0)^{-\gamma}$, where r_0 , the correlation length, is defined so that $\xi_{\text{AA}}(r_0) = 1$ (e.g., Cappelluti et al. 2012). The $\xi_{\text{AA}}(r)$ will depend on both z , luminosity and, possibly, AGN type, but for clarity only the spatial dependence is indicated. Observations typically measure the projected correlation function $w(r_p)$ (where r_p is the projected distance

between a pair of AGNs in the plane of the sky), which is related to the 'real-space' $\xi_{\text{AA}}(r)$ via (Davis & Peebles 1983)

$$w(r_p) = 2 \int_{r_p}^\infty \frac{r \xi_{\text{AA}}(r)}{\sqrt{r^2 - r_p^2}} dr. \quad (7)$$

Assuming that the true correlation function is $\xi_{\text{AA}} = (r/r_0)^{-\gamma}$ then the observed $w(r_p)$ gives an estimate of r_0 (Davis & Peebles 1983).

In HOD modeling it is useful to decompose the total $\xi_{\text{AA}}(r)$ into a '1-halo' term, ξ_{AA}^{1h} , and a '2-halo' term, ξ_{AA}^{2h} (e.g., Yang et al. 2003):

$$\xi_{\text{AA}}(r) = \xi_{\text{AA}}^{1h}(r) + \xi_{\text{AA}}^{2h}(r). \quad (8)$$

The '1-halo' term represents the contribution to the $\xi_{\text{AA}}(r)$ from pairs of AGNs in a single halo, sometimes called satellite AGNs. Determining this term theoretically requires specifying a model of how galaxies and AGNs are distributed within a halo. The transition between the two terms occurs at $r \sim 1 \text{ h}^{-1} \text{ Mpc} < r_0$ for most AGN correlation functions (Cappelluti et al. 2012), so the '1-halo' term will be ignored for determining the CLF (similarly, satellite AGNs were not considered in models developed by Croton (2009) and Conroy & White 2013). Thus, $\xi_{\text{AA}} \approx \xi_{\text{AA}}^{2h}$.

As the '2-halo' term denotes the clustering of AGNs in separate haloes, then they can clearly be related to the clustering of the haloes themselves,

$$\xi_{\text{AA}}^{2h}(r) \approx \bar{b}_A^2 \xi_{\text{dm}}^{2h}, \quad (9)$$

where ξ_{dm}^{2h} is the 'two-halo' contribution to the total dark matter correlation function (defined as $\xi_{\text{dm}}^{2h} = \xi_{\text{dm}} - \xi_{\text{dm}}^{1h}$), and

$$\bar{b}_A = \frac{\int_0^\infty n(M_h) \langle N(M_h) \rangle b(M_h) dM_h}{\int_0^\infty n(M_h) \langle N(M_h) \rangle dM_h} \quad (10)$$

is the mean AGN bias at a specified z . Since $\langle N(M_h) \rangle$ can be computed for any interval in luminosity (Eq. 2), the AGN bias (and therefore the correlation lengths) can also be calculated as a function of luminosity. The $b(M_h)$ factor in Eq. 10 is the bias of dark matter haloes to the underlying dark matter distribution and depends on the definition of 'halo' that is adopted.

At this point the path toward determining the CLF for a sample of AGNs is laid out once a specific cosmological model is chosen. Given a parameterization of the CLF, and the XLF and $r_0(L)$ data for the sample in question, predictions for the AGN correlation lengths and XLF can be computed using the above equations and compared with the data. A fitting technique can then be used to constrain the parameters of the CLF. As seen above, the procedure involves several quantities that depend only on the cosmological model. The details of how these are computed in this paper can be found in Appendix A. The next Section applies this technique to two samples of AGNs, one at $z \approx 0$ and one at $z \approx 0.9$.

3 APPLICATION TO AGN DATA

To determine the CLF of a sample of AGNs using the above framework requires measurements of both the XLF and $r_0(L)$ of the objects in the sample. Due to the relatively small survey areas probed in the 2–10 keV band, this last quantity

has been rarely measured. However, there are determinations of $r_0(L)$ at two different redshifts ($z \approx 0$ and $z \approx 0.9$) which, despite their relatively narrow luminosity range, can be used to illustrate the insights into AGN evolution gained from the CLF methodology.

In the calculations described below, rest-frame 2–10 keV luminosities, L , are computed on a grid from $\log(L/\text{erg s}^{-1}) = 41.11$ to 48 in 531 equally spaced logarithmic steps. The grid of halo masses spans $\log(M_h/M_\odot) = 3$ to 16.473 in 1000 steps. For computational simplicity, Eq. A1 is used to generate a grid of radii from the halo masses on which to calculate correlation functions. This grid extends from ~ 1 pc to ~ 57 Mpc at $z = 0$, but, due to the increase in density at higher z , the maximum radius at $z = 0.9$ is ≈ 20 Mpc. These upper limits in radii cause the predicted $w(r_p)$ to roll off at $r_p \approx 10$ Mpc (see Eq. 7); however, most of the $w(r_p)$ data we compare to are at much smaller projected radii and the predictions of $r_0(L)$ are independent of the $w(r_p)$ calculation. Therefore, given the appropriate datasets, this setup allows for a well-determined measurement of the AGN CLF.

3.1 The $z \approx 0$ Dataset

For AGNs in the local Universe there is a measurement of r_0 in two different luminosity ranges from the 3-year *Swift*-BAT catalog (Cappelluti et al. 2010). The high luminosity value ($r_0 \approx 20$ Mpc) is likely overestimated, as it suggests that local quasars are found in cluster-sized haloes, in contrast to observations (Kauffmann et al. 2004; Popesso & Biviano 2006; Martini et al. 2013). Nevertheless, it is still useful to consider these data because the lower-luminosity point is more accurate, and any luminosity-dependence derived from the CLF model may be instructive.

As a further constraint on the CLF, we use the 6 $w(r_p)$ points at $2 h^{-1}\text{Mpc} \lesssim r_p \lesssim 14 h^{-1}\text{Mpc}$ calculated by Cappelluti et al. (2010) which use the entire luminosity range of their sample. Values of $w(r_p)$ at larger radii are omitted from the fits because of the roll-over described above (the data at these projected radii also lie significantly above the best fit power-law to $w(r_p)$ and thus may be overestimated). The data at smaller projected radii will have a non-negligible contribution from $\xi_{\text{AA}}^{1h}(r)$ which is not modeled by the CLF.

The CLF is determined for 2–10 keV luminosities, while the Cappelluti et al. (2010) data is measured in the *Swift*-BAT 15–55 keV band. An average AGN spectral energy distribution (SED) consisting of a cutoff power-law and reflection spectrum is used to convert between the two bands. SEDs are computed for a range of photon indices ($\Gamma = 1.4$ – 2.4) and then Gaussian averaged with a mean $\Gamma = 1.9$ and $\sigma = 0.3$ to obtain the final SED. An e-folding energy of 250 keV is used for all spectra. Reflection is included using the PEXMON model (Nandra et al. 2007) available in XSPEC (Arnaud 1996) and is added to each power-law prior to averaging so that the Fe $K\alpha$ equivalent width is 120 eV. The final SED is consistent with observations of many samples of local AGN (e.g., Burlon et al. 2011) as well as the average spectrum derived by fitting the local XLFs (Ballantyne 2014). The total luminosity range covered by the Cappelluti et al. (2010) $w(r_p)$ data is estimated to be $42.4 < \log(L_{15-55 \text{ keV}}/(\text{erg s}^{-1})) < 43.9$ which, according to the AGN template, corresponds to $42.25 < \log(L_{2-10 \text{ keV}}/(\text{erg s}^{-1})) < 43.75$.

The $z \approx 0$ 2–10 keV XLF data is taken from Ueda et al. (2014) and Della Ceca et al. (2008). The reason for including the Della Ceca et al. (2008) estimate (which is a de-evolved measurement and therefore model dependent) is that X-ray background synthesis models employing the Ueda et al. (2014) XLF overpredict the local *Swift*-BAT number counts (Aird et al. 2015b; Harrison et al. 2015). Noting this problem, Ballantyne (2014) provided a corrected local 2–10 keV XLF that lies between the Ueda et al. (2014) and Della Ceca et al. (2008) data, but will also fit the *Swift*-BAT number counts. Thus, a more accurate measurement of the local AGN population is obtained by including both the Ueda et al. (2014) and Della Ceca et al. (2008) XLF datapoints. A negative consequence of this decision is that, because the two XLFs are offset for each other, a single XLF model will be a poor statistical fit to these data. Combining these two XLF measurements with the correlation measurements described above yields 32 datapoints available for fitting the CLF.

Now that the necessary data are collected, a form for the AGN CLF must be decided upon and parameterized. As the CLF is statistical in nature, there is freedom to fix the form so that it ‘makes sense’. For example, the XLF at most redshifts is well described by a broken power-law, so integrating the CLF over halo mass (e.g., Eq. 1) should give a broken power-law. Similarly, HOD modeling of AGNs indicate that $\langle N(M_h) \rangle$ also has a roughly power-law shape (Chatterjee et al. 2013; Leauthaud et al. 2015), so integrating the CLF over luminosity (e.g., Eq. 2) also should yield a power-law. This power-law, however, cannot rise indefinitely, so a cutoff halo mass that can depend on AGN luminosity should be included. These considerations lead to the following form for the AGN CLF:

$$\Psi(L|M_h) = \left(\frac{M_h}{M_*}\right)^a e^{-M_h/M_{\text{cut}}} f(L) \quad (11)$$

where

$$M_{\text{cut}} = \left(\frac{L}{L_*}\right)^c M_N, \quad (12)$$

and

$$f(L) = \begin{cases} \left(\frac{L}{L_*}\right)^{-0.96} & \text{if } L < L_* \\ \left(\frac{L}{L_*}\right)^{-\beta} & \text{otherwise.} \end{cases} \quad (13)$$

Fixing the low luminosity slope at -0.96 (equal to the low-luminosity slope of the Ueda et al. 2014 XLF) leaves 6 free parameters to constrain by fitting the XLF and correlation data: a , M_* , β , L_* , c , and M_N . We can simplify the process slightly by noting that, although the mass function $n(M_h)$ is defined down to $1000 M_\odot$, galaxies (and therefore AGNs) are not typically found in haloes with $M_h \lesssim 10^9 M_\odot$ (e.g., Efstathiou 1992; Benson et al. 2002; Nickerson et al. 2011; Shen et al. 2014); thus, $\Psi(L|M_h) = 0$ for those masses. Other assumed forms for the CLF (e.g., log-normals, power-laws, exponentials) did not provide acceptable fits to the XLF data. While more complex forms could provide equally good fits to the data, the parameterization shown above appears to be the simplest CLF description supported by the available data. Of course, as additional $r_0(L)$ data becomes available, particularly at higher luminosities, this parameterization may have to be revised.

3.2 The $z \approx 0.9$ Dataset

Koutoulidis et al. (2013) measured $r_0(L)$ in two luminosity ranges for AGNs at $z \sim 0.9$ –1 in five different deep X-ray surveys, yielding 10 different measurements of $r_0(L)$. The values of r_0 determined from the *Chandra* Deep Field South are much larger than the other fields (likely due to the large supercluster in the field) and is omitted from the CLF fits. Specifically, we use the r_0 data in the CLF model, and not the ‘corrected’ $r_{0,c}$ values listed by Koutoulidis et al. (2013) that attempts to account for the finite area of the surveys. In practice, these two estimates of the correlation length are almost always consistent within the errors. As with the $z \approx 0$ field, the $r_0(L)$ data is augmented with the $w(r_p)$ profile measured by Koutoulidis et al. (2013) using their entire $z \approx 0.9$ sample with the measurements at the largest and smallest r_p omitted in the calculations for the reasons described above. Finally, Koutoulidis et al. (2013) work with luminosities in the 0.5–8 keV band, and the same AGN SED described for the $z \approx 0$ data is used to convert these into the 2–10 keV band. Therefore, the Koutoulidis et al. (2013) $w(r_p)$ data, that spans $41.25 \lesssim \log(L_{0.5-8 \text{ keV}}/(\text{erg s}^{-1})) \lesssim 44.5$, converts to the range $41.1 < \log(L_{2-10 \text{ keV}}/(\text{erg s}^{-1})) < 44.3$. The XLF data for the CLF fitting is taken from the $z = 0.8$ –1.0 panel in the Ueda et al. (2014) measurement of the evolving XLF. Combining the Ueda et al. (2014) XLF data points with the Koutoulidis et al. (2013) correlation function data gives a total of 26 data points with which to constrain Eqs. 11–13.

Determining the CLF at this redshift involves calculations of $n(M_h)$ and ξ_{dm} at one z (namely, $z = 0.9$) while the data that is constraining the CLF has been gathered over a range of redshift (e.g., $z \approx 0.7$ –1.1 for the correlation data; Koutoulidis et al. 2013). In principle, this mismatch may lead to an inaccurate measurement of AGN properties at $z = 0.9$. As shown by van den Bosch et al. (2007) and described in Appendix B, the CLF equations can be adapted so that an ‘effective’ $n(M_h)$ and ξ_{dm}^{2h} , defined over the necessary z range, is used in place of the ones calculated at a single redshift. In practice, this correction is too small for the redshift range applicable here, and so is not used for the current calculation.

3.3 Fitting the Data

For both redshifts, the 6 CLF parameters are determined by minimizing the total χ^2 from all data points using the Metropolis algorithm (Metropolis et al. 1953) to ensure that the true global minimum is found. To obtain $\chi^2/\text{dof} \approx 1$ (dof=degree of freedom) we used the larger of the two errorbars in the XLF datapoints, but otherwise used the smallest ones for the $w(r_p)$ and r_0 data. This procedure assumes that all the errorbars are independent and Gaussian distributed. The best fitting CLF parameters are shown in Table 1, where the uncertainties are the 90% confidence level for one degree of freedom (i.e., a $\Delta\chi^2 = 2.71$ criterion). Due to including two non-compatible measurements of the $z \approx 0$ XLF, the χ^2 of the CLF fit is formally poor. Fitting only to the Ueda et al. (2014) XLF yields a $\chi^2/\text{dof} = 0.96$; however, the quantities derived from the CLF will be more accurate after including the Della Ceca et al. (2008) XLF estimate.

As the CLF is a statistical quantity, one has to be careful not to overinterpret the numbers in the Table. Never-

theless, there are some trends that one can glean from examining the CLF fits. For example, the overall luminosity scale increase with z , as observed in the evolution of the XLF (e.g., Ueda et al. 2014; Aird et al. 2015a). The mass scale, as measured by M_* and M_N also increases, although this is not typically inferred from X-ray clustering measurements (Cappelluti et al. 2012). Interestingly, the parameters that quantifies the coupling between the halo mass and the AGN luminosity (c) is $\approx 2\times$ lower at $z \approx 0.9$ than at $z \approx 0$.

Figures 1 and 2 show how well the best-fit CLFs recover the observed XLF, $w(r_p)$ and r_0 in both redshift bins. To illustrate the reliability of the results, the 95% confidence regions, which is a $\Delta\chi^2 = 12.59$ criterion for 6 degrees of freedom, is indicated in all plots. The confidence regions are computed using a Monte-Carlo approach. Beginning at the best-fit indicated in Table 1, one of the six parameters is increased or decreased by at most 0.02, and a new χ^2 is calculated. If this χ^2 is within the confidence limit then the parameters are stored, and a new random change to the parameters is made. After each parameter has been randomly adjusted on average 500 times, the parameters are reset to the best-fit and the process is restarted. This whole procedure is done 10 times for each fit, resulting in 2569 models within the confidence region at $z \approx 0$ and 2182 models at $z \approx 0.9$. Then at $z \approx 0$, for each L (in the case of $\phi(L)$ or $r_0(L)$) or each r (in the case of $w(r_p)$), the CLF model is computed for each of the 2569 set of parameters, and the minimum and maximum $\phi(L)$, $r_0(L)$ and $w(r_p)$ are determined. These minima and maxima determine the 95% confidence regions shown in the figures. The same process is repeated to calculate the $z \approx 0.9$ confidence levels.

In addition to the XLF data, the $z \approx 0$ panel also shows the best-fit XLF as determined by Ballantyne (2014) from fitting the XLFs in multiple energy bands. This fit (as shown by the red long dashed line) can account for all the local AGN demographics, including the *Swift*-BAT data. Although derived from a completely independent process, the CLF-derived XLF (solid line) matches the Ballantyne (2014) measurement very well, particularly around the knee of the XLF. This agreement gives us confidence that the CLF model can be used to obtain accurate information on the AGN population.

4 RESULTS DERIVED FROM THE AGN CLFS

In this section, we explore the statistics of various AGN physical quantities derived from the CLF at these two redshifts, and discuss the implications for our understanding of AGN evolution at different luminosities.

4.1 AGN Bias and Mean Halo Mass

The first two statistical properties of AGNs we will consider are the mean AGN bias, \bar{b}_A (Eq. 10), and the mean mass of AGN-hosting haloes, $\langle M_h \rangle$ (Eq. 3). Figure 3 plots the 95% confidence regions for these two quantities for both $z \approx 0$ and $z \approx 0.9$. There is a significant luminosity dependence to both quantities at each redshift that arises from the observed behaviour of $r_0(L)$. As a result, for both \bar{b}_A and $\langle M_h \rangle$, there seems to be a transition in behaviour at a luminosity of $\log(L/(\text{erg s}^{-1})) \approx 44$. Above that luminosity, the

Table 1. Best-fit AGN CLF parameters at $z \approx 0$ and $z \approx 0.9$ (Eqs. 11–13). The error-bars are calculated using a $\Delta\chi^2 = 2.71$ criterion (i.e., a 90% confidence level for the parameter of interest).

Redshift	χ^2/dof	a	$\log(M_*/M_\odot)$	β	$\log(L_*/\text{erg s}^{-1})$	c	$\log(M_N/M_\odot)$
0	58.04/26	2.20 ± 0.05	12.51 ± 0.04	$2.57^{+0.05}_{-0.04}$	41.79 ± 0.05	$1.27^{+0.07}_{-0.06}$	12.33 ± 0.08
0.9	12.77/20	$2.96^{+0.08}_{-0.10}$	$14.43^{+0.04}_{-0.03}$	$3.26^{+0.88}_{-0.42}$	44.47 ± 0.05	$0.59^{+0.05}_{-0.04}$	$15.20^{+0.07}_{-0.08}$

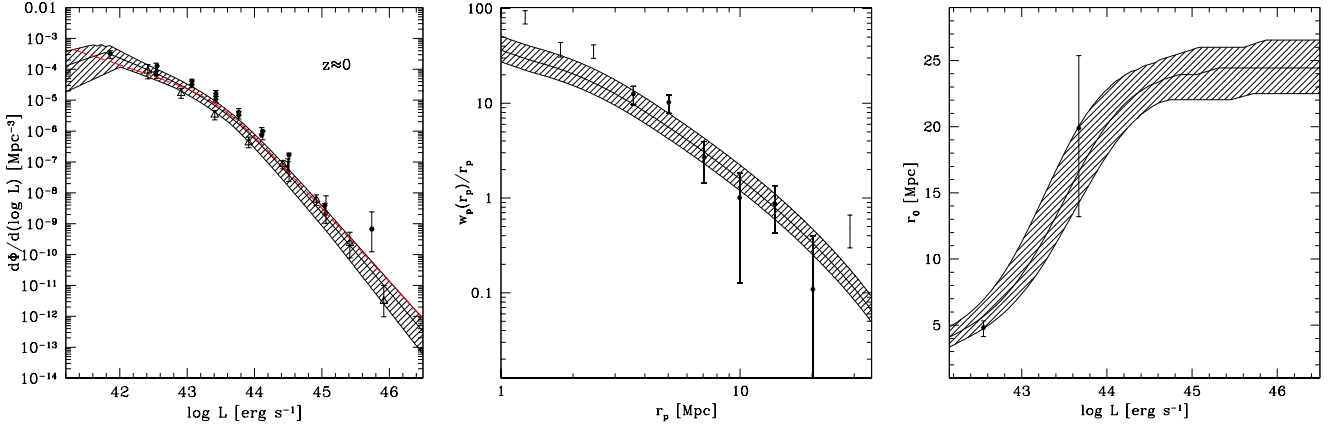


Figure 1. Fits to the $z \approx 0$ XLF (left), $w(r_p)$ (middle) and r_0 (right) data that determined the AGN CLF at this redshift. In all plots the solid line indicates the prediction from the best-fit CLF (top row of Table 1), and the hatched region shows the 95% confidence region on this quantity. In the XLF plot, the solid points denotes data taken from the paper of Ueda et al. (2014) and the triangles are the Della Ceca et al. (2008) estimate of the local LF. The red dashed line in the XLF panel plots the best-fit $z=0$ XLF determined by Ballantyne (2014) from fitting the local XLFs in multiple energy bands. The $w(r_p)$ and r_0 data of Cappelluti et al. (2010) are shown in the other two panels, with the solid points indicating ones that are actually used in the CLF fit (the other points are omitted from the fit; see text for details).

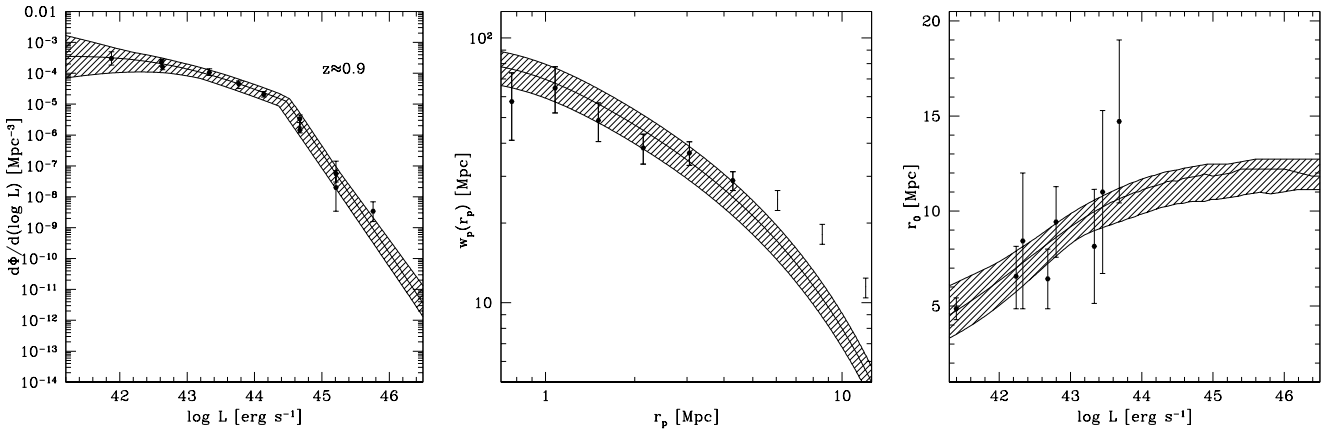


Figure 2. As in Fig. 1, but at $z \approx 0.9$. In this case, the $w(r_p)$ and r_0 data are taken from Koutoulidis et al. (2013). The parameters of the best-fit CLF are listed in the bottom row of Table 1.

mass of AGN-hosting haloes is approximately constant, in agreement with surveys that show little-to-no luminosity dependence in the clustering of quasars (e.g., Shen et al. 2013; Eftekharzadeh et al. 2015). This indicates that these high-luminosity AGNs have a common triggering mechanism that depends only on being in a certain, highly biased, environment. The wide span of luminosity over which the mass is roughly constant can be interpreted by invoking a range of black holes masses and the fact that that all AGNs exhibit significant variability (e.g., Hickox et al. 2014). In contrast,

at $\log(L/(\text{ergs}^{-1})) \lesssim 44$ AGN triggering must be occurring by a process that depends on halo mass. Moreover, the lower bias means that these AGNs do not need to inhabit significantly dense environments and can therefore be triggered by processes internal to the host halo, such as accretion from the halo itself (e.g., Fanidakis et al. 2013). Interestingly, the $z \approx 0.9$ luminosity-dependence is weaker than at $z \approx 0$ which likely means that there is a larger fraction of AGNs triggered in massive haloes at all luminosities during this epoch. Such environments are more conducive to galaxy interactions and

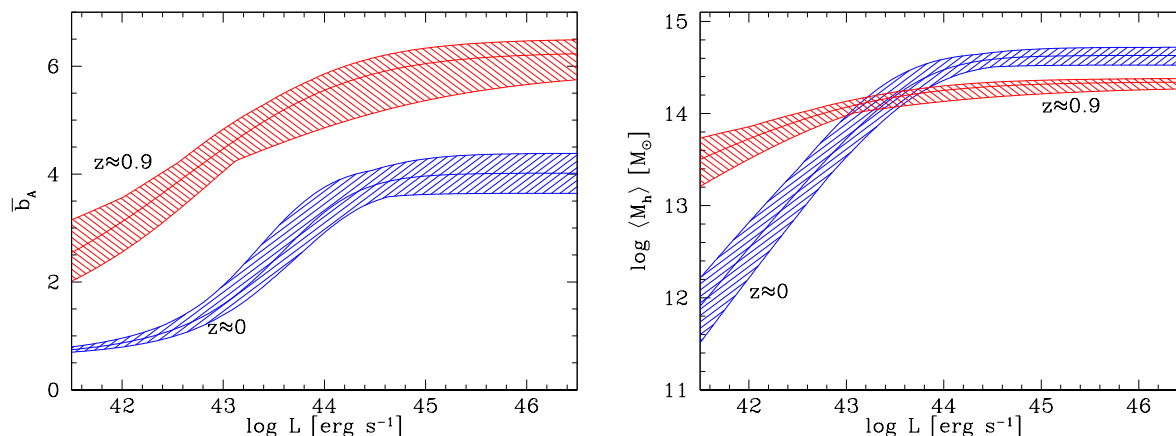


Figure 3. The CLF-derived AGN bias, \bar{b}_A (left), and mean halo mass, $\langle M_h \rangle$ (right), as a function of AGN X-ray luminosity at $z \approx 0$ (blue) and $z \approx 0.9$ (red). The solid lines are the predicted values, and the surrounding hatched areas are the 95% confidence regions. Both quantities exhibit significant increases with luminosity, in particular at $\log(L/(\text{erg s}^{-1})) \lesssim 44$. This result likely indicates that different AGN fueling mechanisms are operating at high and low luminosities. The luminosity dependence is weaker at $z \approx 0.9$ which may be linked to a switch between merger-dominated and secularly-triggered AGN growth (e.g., Draper & Ballantyne 2012). The large values of \bar{b}_A and $\langle M_h \rangle$ predicted for local quasars result from the high- L r_0 point of Cappelluti et al. (2010) and are therefore likely to be overestimated.

mergers, and gas-rich galaxies are more common at higher redshifts, thus these results indicate that AGN triggering by major mergers is more common at $z \sim 1$ and becomes much rarer at low z (e.g., Salucci et al. 1999; Draper & Ballantyne 2012).

The average bias and mean halo mass of $z \approx 0$ quasar hosts appears unrealistically large, as they imply local quasars should reside in nearby massive clusters, which is not observed (e.g., Martini et al. 2013). The large values result from fitting the high- L r_0 point from Cappelluti et al. (2010) and therefore appears to be overestimated. That analysis relied on the 3-year *Swift*-BAT catalog with only 199 AGNs. The latest *Swift*-BAT catalog by Baumgartner et al. (2013) contains over 600 AGNs, so an update to the clustering analysis should give significant improvements to the local CLF model. In contrast, the $z \approx 0.9$ results show that quasars at that redshift might be commonly found in haloes with $\log(M_h/M_\odot) \approx 14 - 14.3$, corresponding to large groups or young clusters at this redshift. This result will be discussed further in Sect. 5.2.

A related view of these relationships can be obtained by calculating the mean AGN luminosity as a function of halo mass, $\langle L \rangle(M_h)$, via

$$\langle L \rangle(M_h) = \frac{\int L \frac{d\Phi}{d\log L}(L, M_h) d\log L}{\int \frac{d\Phi}{d\log L}(L, M_h) d\log L}, \quad (14)$$

where

$$\frac{d\Phi}{d\log L}(L, M_h) = \Psi(L|M_h)n(M_h)dM_h \quad (15)$$

is the XLF for AGNs in haloes with mass M_h . Figure 4 plots the results for the CLFs derived at $z \approx 0$ and 0.9. The mean AGN luminosities at both $z \approx 0$ and 0.9 increases with halo mass, as long as $\log(M_h/M_\odot) \gtrsim 12$ (for $z \approx 0$) or 13 ($z \approx 0.9$). The slopes of the relations also differ substantially. At $\log(M_h/M_\odot) > 12.5$, we find $L \propto M_h^{0.8}$ at $z \approx 0$, although this slope may be an overestimated due to the large Cappelluti et al. (2010) r_0 point causing high- L AGNs to inhabit massive haloes. At $z \approx 0.9$, the slope is measured for

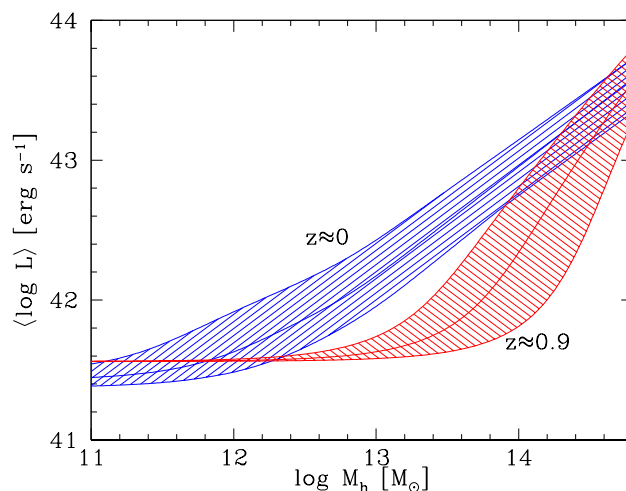


Figure 4. The average AGN luminosity as a function of halo mass at $z \approx 0$ (blue line and hatched region) and $z \approx 0.9$ (red line and hatched region). In both cases, the average luminosity increases with mass, but only above a halo mass of $\log(M_h/M_\odot) \approx 12$. The slopes are also different (≈ 1.2 at $z \approx 0.9$; ≈ 0.8 at $z \approx 0$), indicating that the local AGN population is more spread out in haloes of different masses.

$\log(M_h/M_\odot) > 13.5$, and we find $L \propto M_h^{1.2}$. The slope at $z \approx 0$ appears to be in good agreement with the results of a similar analysis by Hütsi et al. (2014), but the $z \approx 0.9$ slope is much steeper than their result at the same redshift. This difference most likely arises from the assumption made by Hütsi et al. (2014) that the power-law relation between luminosity and halo mass spans the entire range in mass. Similarly, the slope of 1.2 at $z \approx 0.9$ is not very different from the slope of 1.4 predicted by Croton (2009), but, as the AGN triggering physics has changed, the flatter slope at $z \approx 0$ is not consistent with the Croton (2009) model.

Figure 4 shows that at $z \approx 0.9$ the average AGN luminosity is nearly constant with halo mass until $\log(M_h/M_\odot) \approx$

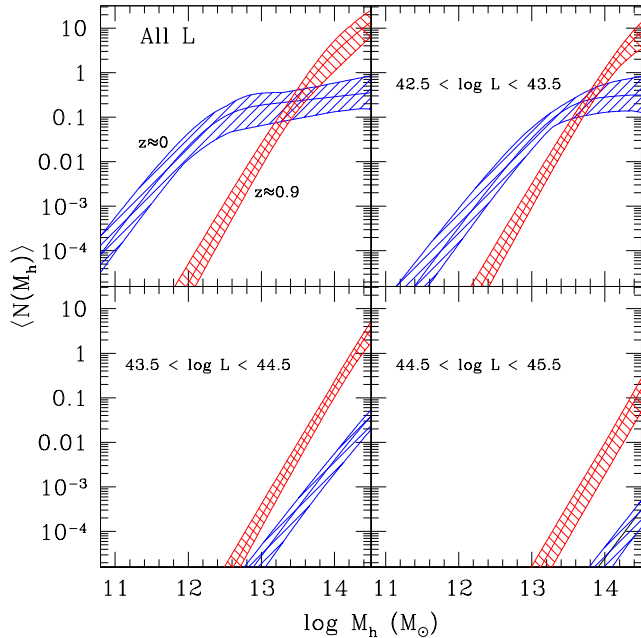


Figure 5. The CLF-derived mean halo occupation number of AGNs at $z \approx 0$ and 0.9 in four different luminosity ranges. The solid lines are the predicted values with the hatched regions denoting the 95% confidence limits. As the CLF model only treats the ‘2-halo’ term of the correlation function, these predictions are unable to distinguish between central and satellite AGNs.

13. This means that in less massive haloes, the average AGN luminosity is independent of the hosting halo mass, consistent with either the fading of previously triggered quasars, or a form of triggering by secular processes (Draper & Ballantyne 2012). This behaviour is roughly consistent with the instantaneous $z = 1$ $L - M_h$ relation found by Chatterjee et al. (2011) using a hydrodynamical simulation of AGN evolution. Above $\log M_h \approx 13$, the mean AGN luminosity increases steeply with halo mass, implying only these massive haloes can produce AGNs that are, on average, typical of quasars. Interestingly, at $z \approx 0$ the average AGN luminosity depends on halo mass over a broad range of masses. In the local Universe, AGNs can be found in a variety of environments since they are likely triggered by a variety of internal processes that may operate on a wide range of timescales. At both redshifts the mean AGN luminosity is often significantly lower than the typical quasar value of $\log(L/(\text{erg s}^{-1})) \approx 44$; this, of course, follows from the XLF which shows that at these redshifts, lower luminosity AGNs dominate the space density.

4.2 AGN Halo Occupation

The average number of AGNs occupying haloes of different masses, $\langle N(M_h) \rangle$, allows another view into the triggering and evolution of AGNs in their cosmological environment. Figure 5 shows the CLF predictions for $\langle N(M_h) \rangle$ (computed from Eq. 2) in four luminosity ranges at both $z \approx 0$ and 0.9. Recall that the AGN CLF was constrained using only that part of the correlation function dominated by the ‘2-halo’ term,

so the predicted $\langle N(M_h) \rangle$ contains contributions from both central and satellite AGNs. The satellites will only become relevant for haloes above $\log(M_h/M_\odot) \sim 13.5$ (i.e., group scale or larger; Chatterjee et al. 2011; Leauthaud et al. 2015), and, indeed, it is only for those masses $\langle N(M_h) \rangle > 1$.

At $z \approx 0$, the total AGN occupation number rises quickly from $\log(M_h/M_\odot) \approx 11$ to 12.5 before flattening to a much shallower rise to larger halo masses. In the local Universe, once they are integrated over luminosity, AGNs are found in haloes with $\log(M_h/M_\odot) \gtrsim 12.5$ at roughly equal numbers (roughly, 0.2–0.5 AGNs per halo). This shape is roughly consistent with the results of Leauthaud et al. (2015) who estimate the AGN halo occupation at $0.2 < z < 1$ with $41.5 \lesssim \log(L/(\text{erg s}^{-1})) \lesssim 43.5$. However, considering the AGN population in finer L bins yields occupation distributions that, by construction, are best described as cutoff power-laws. Following the XLF at $z \approx 0$, the occupation number falls quickly with luminosity with quasars occupying only a tiny fraction of haloes.

The shape of the $z \approx 0.9$ AGN occupation curves are similar to the ones at $z \approx 0$, but, following the evolution in the XLF, the curves are shifted so that more luminous AGNs are more numerous. The occupation for all AGNs at $z \approx 0.9$ is greater than unity for haloes at $\log(M_h/M_\odot) \gtrsim 13.8$. These AGNs are mostly luminous Seyferts and quasars, and are found in haloes which are in the process of collapsing (van den Bosch 2002). Clearly, processes in these haloes allow efficient triggering of AGNs that is not found in their lower redshift analogues (Sect. 5.2).

Earlier measurements of the AGN halo occupation find that the shape of the distribution for ‘central’ AGNs is a step or an error function (Chatterjee et al. 2011; Miyaji et al. 2011; Leauthaud et al. 2015), and that the satellite population is best described by a cutoff power-law. In contrast, we find that the occupations distribution of all AGNs is consistent with a cutoff power-law when considered over a narrow luminosity range. After integrating over luminosity and summing up the individual cutoff power-laws, we find a AGN halo occupation distribution that is flatter and more consistent with the step and error functions found by previous authors. This result illustrates the importance of considering the luminosity dependence of the AGNs when describing the halo occupation statistics.

4.3 Average Black Hole Growth Rate

The upper-left panel of Fig. 5 shows the mean number of AGNs of all luminosity in dark matter haloes as a function of halo mass. Multiplying this curve by the average luminosity of AGNs in each AGN-occupying halo (Fig. 4) gives the AGN luminosity averaged over all haloes of a given mass. This quantity therefore gives the average accretion-driven black hole growth rate as a function of halo mass at the given z .

Figure 6 shows the results of this calculation for both redshifts where the average AGN X-ray luminosity is indicated on the left-hand axis and the equivalent average black hole accretion rate (assuming a radiative efficiency of 0.1 and a bolometric correction of 30; Vasudevan & Fabian 2009) is noted on the right-hand axis. There is a marked difference between the two epochs. At $z \approx 0.9$, black hole growth is strongly weighted to higher mass haloes, where both the oc-

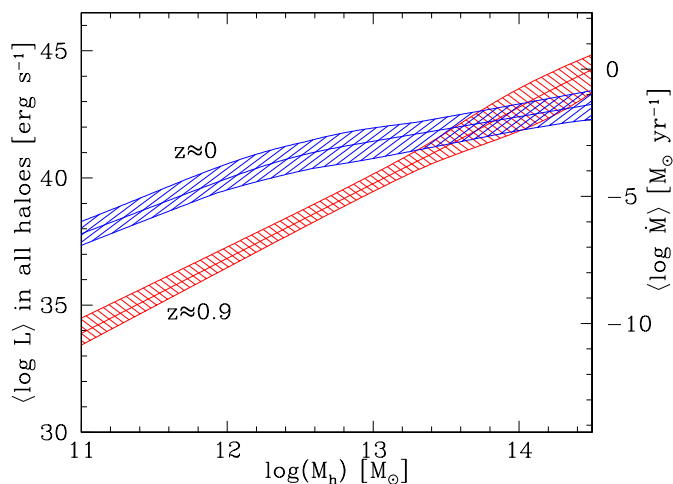


Figure 6. Average AGN luminosity produced by all dark matter haloes as a function of halo mass. The right-hand axis translates this to an average black hole growth rate in haloes after assuming a radiative efficiency of 0.1 and a bolometric correction of 30 (Vasudevan & Fabian 2009). At $z \approx 0.9$ the vast majority of the black hole growth occurs in high mass haloes. However, the black hole growth in lower mass haloes increases by several orders of magnitude from $z \approx 0.9$ to $z \approx 0$, consistent with the concept of cosmic downsizing.

cupation number and mean luminosity of AGNs are large, while black holes in haloes with masses $\log(M_h/M_\odot) \lesssim 13$ are growing very slowly. It seems that the turbulent environment of a collapsing $\log(M_h/M_\odot) \gtrsim 14$ halo provides numerous mechanisms for the galaxy interactions necessary for the growth of the massive black holes seen in galaxies within nearby clusters. At $z \approx 0$, the growth rate in the lower-mass haloes has risen by several orders of magnitudes, and the rate in the high mass haloes has fallen. Overall, this figure nicely illustrates the ‘cosmic downsizing’ (e.g., Hasinger et al. 2005; Bundy et al. 2006; Ueda et al. 2014) concept where the most massive black holes and galaxies are grown earlier on in the Universe before the lower mass black holes and galaxies.

4.4 AGN Lifetime

As mentioned in Sect. 2.1, the AGN CLF can be used to estimate the AGN lifetime as a function of luminosity by computing the fraction of haloes that host AGNs at a given luminosity. Since there is a one-to-one correspondence between luminosity and mean halo mass (Fig. 3), each luminosity corresponds to a mean mass from which the space density of haloes at that mass can be computed (Eq. 5). This estimate of lifetime assumes the halo lifetimes are equal to the Hubble time, which means the AGN lifetimes are, strictly speaking, upper-limits.

The lifetimes computed from our CLF models are shown in Figure 7, with the hatched regions showing the 95% confidence regions. The lifetimes generally fall in the range of 10^7 – 10^8 yrs, except at the highest luminosities. Depending on how one defines quasar, our quasar lifetimes are in good agreement with the predictions from the semi-analytical models of Croton (2009) and Conroy & White (2013) as well

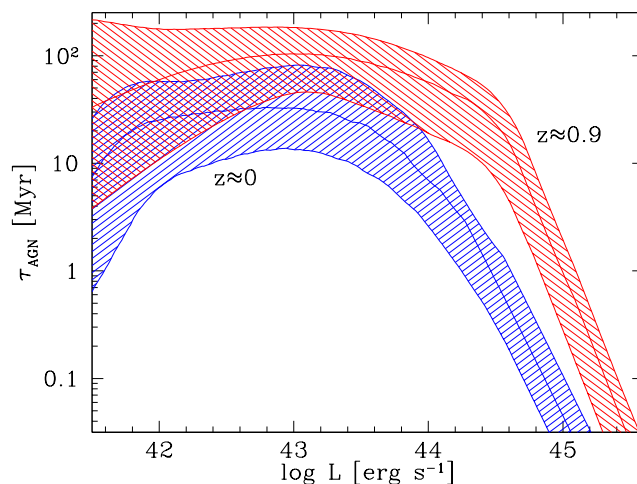


Figure 7. AGN lifetimes at $z \approx 0$ and 0.9 estimated from Eq. 5 and the best-fitting CLF models. The hatched regions denote the 95% confidence levels around the predicted lifetimes (solid lines). As with the other statistics, there is a strong luminosity dependence to the lifetimes, with lower luminosity AGNs exhibiting longer lifetimes than the higher luminosity quasars.

as the range of estimates found from a variety of methods (Martini 2004). At both redshifts, the lifetimes exhibit a significant luminosity dependence, with the lifetimes falling at high luminosities. This shape follows from the shape of the XLF and is consistent with other estimates of the quasar lifetime (Croton 2009). At lower-luminosities, more consistent with Seyfert galaxies, the lifetimes are roughly constant with luminosity. The transition in lifetimes again indicates the two modes of AGN fueling physics that operates at low and high luminosity.

4.5 How to Populate Haloes with AGNs in Numerical Simulations

Despite rapid progress in technology, cosmological simulations continue to have difficulty accurately capturing the detailed physics of AGN fueling and feedback because of the small size and time scales that must be resolved during the calculation (e.g., Springel et al. 2005; Sijacki et al. 2015). As a result, there remains considerable uncertainty in how well the simulated AGN population resembles the actual one, particularly with regards to AGN fueling, appearance (e.g., obscured versus unobscured) and lifetimes (e.g., Hopkins et al. 2014; Cen & Safarzadeh 2015). This uncertainty ultimately impacts theories of how AGN activity affects galaxy evolution. Many cosmological calculations use the technique of ‘abundance matching’ (e.g., Conroy, Wechsler & Kravtsov 2006; Croton 2009) to ensure the AGN luminosity function is followed; however, how these AGNs are assigned to different halo masses or given luminosities is extremely model dependent. The CLF methodology developed here, which naturally gives relationships between luminosity and halo mass (e.g., Fig. 3), provides a more observationally motivated way of assigning AGNs to numerical haloes. Below, we use the $z \approx 0.9$ AGN CLF derived above to illustrate three ways the CLF can assist cosmological simulations in their treatment of AGNs.

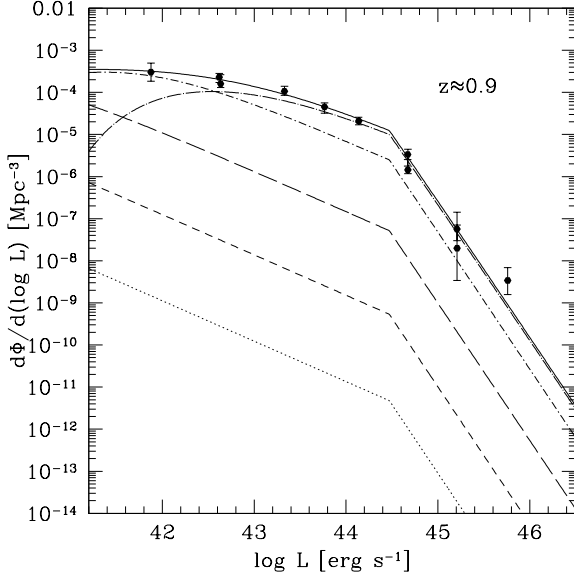


Figure 8. The contribution to the $z \approx 0.9$ XLF from AGNs hosted by dark matter haloes of various masses. The data points and the solid line are the same as in Fig. 2. The other lines indicate the XLF from AGNs hosted by haloes with $\log(M_h/M_\odot) < 11$ (dotted), $11 < \log(M_h/M_\odot) < 12$ (short dashed), $12 < \log(M_h/M_\odot) < 13$ (long dashed), $13 < \log(M_h/M_\odot) < 14$ (short dash-dotted), and $14 < \log(M_h/M_\odot)$ (long dash-dotted).

The first possibility is to update the idea of abundance matching by considering the halo mass dependence of the XLF. This is shown in Figure 8 where the derived CLF at $z \approx 0.9$ is used to compute XLFs for different ranges of M_h . This plot encapsulate many of the results presented above; namely, the transition in halo host mass at $\log(L/(\text{erg s}^{-1})) \sim 44$. These halo-dependent XLFs will provide crucial new information to modelers when populating AGNs in numerical haloes by matching the observed luminosity function.

An alternative way of doing the assignments of AGNs numerically is through probabilities, and by using the CLF we can calculate the AGN halo mass probability density function (Leauthaud et al. 2015), defined as

$$f_{\text{AGN}} = \frac{\langle N(M_h) \rangle n(M_h)}{\int \langle N(M_h) \rangle n(M_h) dM_H}. \quad (16)$$

This quantity, which is plotted for $z \approx 0$ and 0.9 in Figure 9, shows how probable it is for AGNs to be hosted by haloes of a given mass, and can be used in conjunction with the traditional abundance matching technique. As long as the computed halo mass function is compatible with the Tinker et al. (2010) used here, then populating haloes with these probability density functions should automatically reproduce the AGN XLF at the appropriate redshift.

The luminosity-dependent AGN correlation function is a further constraint to the AGN population that has not often been used when populating haloes. In Fig. 10, the CLF-predicted $\xi_{\text{AA}}(r)$ for $z \approx 0.9$ AGNs in different luminosity bins are plotted. As found by observations (Koutoulidis et al. 2013), the correlation length increases with luminosity, and this behavior is captured by the CLF. Combining these correlation functions with either of the two changes to the abundance matching techniques described above will allow cos-

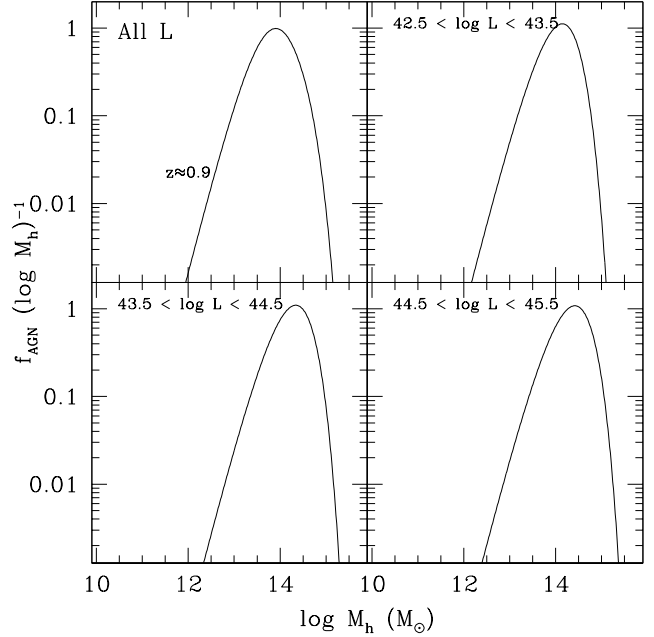


Figure 9. AGN halo mass probability density function (Eq. 16) in different luminosity bins at $z \approx 0.9$. This type of plot can be used to populate AGNs with the appropriate luminosities in dark matter haloes in cosmological simulations.

mological models to more accurately include the effects of AGNs in the growth of galaxies in a more observationally-rigorous manner. For example, once the CLF results are used to populate AGNs in haloes at a specific z , the simulation can be used to examine the history or future of those haloes, and make predictions for how the clustering and fueling of those AGNs have changed or will change with time.

5 DISCUSSION

5.1 AGNs in their Cosmological Environments: Luminosity-Dependence

The central aspect of the CLF methodology is that it naturally produces a luminosity-dependent AGN HOD model. However, measurements of $r_0(L)$ are necessary in order to constrain the CLF, and therefore the predictions derived from the CLF are limited by the number and accuracy of these measurements. Despite this limitation, there is substantial interest in whether the environment of AGN host galaxies is connected to AGN observational characteristics such as luminosity and obscuration. The CLF is a valuable tool to examine these questions, especially as further $r_0(L)$ measurements become available over the next decade.

We have decided to use X-ray survey data to constrain and study the AGN CLF despite the relatively limited number of datasets available compared to studies of optical quasars. This was done because X-ray surveys provide a view of the AGN population that is both unbiased to Compton-thin obscuration and covers a substantial range in luminosity. Optical quasar surveys are effective in sampling the high- z , unobscured AGN population, but are typically sensitive

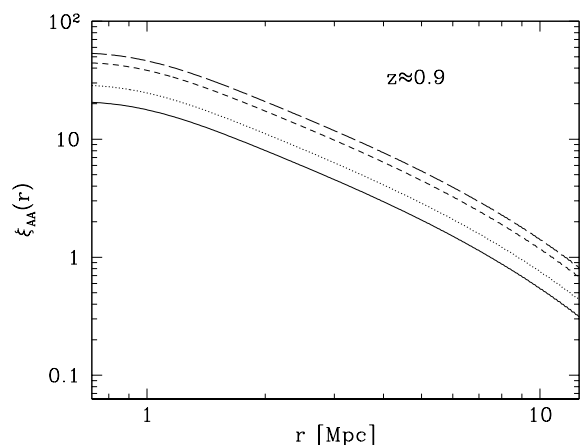


Figure 10. Predictions for the AGN 2-point correlation function, $\xi_{AA}(r)$, at $z \approx 0.9$. The different curves differentiate between AGNs at different X-ray luminosities: $42.5 < \log(L/(\text{ergs}^{-1})) < 43.5$ (dotted), $43.5 < \log(L/(\text{ergs}^{-1})) < 44.5$ (short-dashed), $44.5 < \log(L/(\text{ergs}^{-1})) < 45.5$ (long-dashed), and integrated over all L (solid). The XLF of AGNs shows that the space density of AGNs is dominated by lower-luminosity objects, so the integrated $\xi_{AA}(r)$ is closer to the curve for the lower-luminosity bin. These are ‘2-halo’ correlation functions, and are therefore cutoff at small separations.

to a narrower range in luminosity than what is found in X-ray surveys (e.g., [Krumpe et al. 2015](#)). As we are specifically interested in examining the luminosity dependence of the host halo properties, the X-ray data provides the best constraints. However, as pointed out by [Leauthaud et al. \(2015\)](#), the data products produced by X-ray AGN surveys may also be biased to more massive host galaxies, as only these will be luminous enough to obtain a redshift measurement. This effect may influence the inferred masses of AGN hosting haloes.

Bearing this caveat in mind, the results of the previous section shows that the AGN luminosity does depend on the halo properties at both $z \approx 0$ and 0.9 . This luminosity dependence grows stronger as the Universe ages, and can be reasonably interpreted as demonstrating two different modes of AGN triggering. One mode can generate short-lived high-luminosity quasars at any z ; these objects are rare and therefore typically populate high mass haloes, but, if the environment is correct, the AGN luminosity does not depend on the halo mass. These properties roughly translate into a merger triggered AGN scenario (e.g., [Lidz et al. 2006](#); [Fanidakis et al. 2013](#)). The other mode of AGN triggering becomes prominent at $z \lesssim 0.9$ and produces lower-luminosity AGNs that are much longer-lived, but with luminosities that depend on halo mass. These lower-luminosity AGNs can also be found over a range of different halo mass, and may be triggered by ‘secular’ processes (including disk instabilities, minor mergers, galaxy harassment, halo-gas accretion) that can operate in a wide range of cosmological environments.

The luminosity-dependence of our results makes it challenging to perform quantitative comparisons to previous work. Moreover, differences in assumed cosmology and the $\bar{b}_A \rightarrow M_h$ conversion lead to additional errors when performing comparisons. Therefore, we will focus on a general comparison between our results and those from the literature.

Common values for halo masses found from clustering of X-ray selected AGNs are $\log(M_h/M_\odot) \sim 13 - 13.5$ (independent of z ; [Cappelluti et al. 2012](#)) which is roughly consistent with the CLF-derived results for lower-luminosity AGNs at $z \approx 0.9$, but misses the strong luminosity dependence at $z \approx 0$. [Leauthaud et al. \(2015\)](#) estimate halo masses of moderate luminosity low- z X-ray AGNs using lensing information and find halo masses $\sim 10^{12.5} M_\odot$, which is in rough agreement with our results. Recently, [Mendez et al. \(2016\)](#) measured the clustering of X-ray AGN in two luminosity bins, one with $\langle \log(L/(\text{ergs}^{-1})) \rangle \sim 42.4$ and $\langle z \rangle = 0.57$, and the other with $\langle \log(L/(\text{ergs}^{-1})) \rangle \sim 43.2$ and $\langle z \rangle = 0.87$. For the latter sample, they find $\log(M_h/M_\odot) \sim 13.4$ if they include the COSMOS field, and 13.1 if they omit COSMOS, values that are $\approx 4\times$ lower than the CLF predictions (Fig. 3). In contrast, the lower z and luminosity sample of [Mendez et al. \(2016\)](#) has about the same halo mass and bias as the higher luminosity bin, a result that disagrees with the expectation from the CLF (and the [Leauthaud et al. \(2015\)](#) results).

Interestingly, optically-selected quasars seem to populate haloes with masses about an order of magnitude lower than X-ray select AGNs ([Cappelluti et al. 2012](#)). However, as argued by both [Leauthaud et al. \(2015\)](#) and [Mendez et al. \(2016\)](#) comparing clustering results between AGNs selected at different wavelength leads to strong biases, since the host galaxies properties can be very different between the two samples. For example, as mentioned above, X-ray selected samples may be biased to higher mass galaxies (and hence higher mass haloes) due to the need to obtain host galaxy redshifts. Optical quasars are likewise subject to biases related to the detection of strong emission lines with the correct ratios (e.g [Moran, Filippenko & Chornock 2002](#); [Trump et al. 2015](#)). Thus, a straightforward comparison between the two sets of results is not possible. Future CLF modeling will focus on creating a connection from the X-ray based method to the existing optical clustering measurements at higher redshifts that will test the effects of these biases.

5.2 Luminous AGNs in High Redshift Young Galaxy Clusters

One of the most striking predictions of the AGN CLFs derived here is the cluster-sized masses for haloes hosting luminous AGNs ($\log(L/(\text{ergs}^{-1})) \gtrsim 43$). This prediction is not supported by observations at $z \approx 0$, where luminous AGNs are very rarely found in galaxy clusters, and, indeed, the cluster AGN fraction is smaller than the field fraction ([Galamez et al. 2009](#); [Ehlert et al. 2013](#); [Martini et al. 2013](#)). Thus, even though the halo mass found here agrees with the one inferred by [Cappelluti et al. \(2010\)](#), the large value of r_0 used to constrain the CLF at high luminosity is likely overestimated and therefore giving erroneous results at these luminosities. An update to the *Swift*-BAT clustering analysis would significantly clarify the results for local AGNs.

The situation at $z \approx 0.9$ is significantly different. In fact, there are several lines of evidence that luminous AGNs in $\log(M_h/M_\odot) \sim 14$ haloes are common at $z \sim 1$. First, the fraction of luminous AGNs in clusters rises rapidly with redshift to the point where the fraction appears to be at least equal to that of the field at $z \gtrsim 1$ ([Galamez et al.](#)

2009; Martini et al. 2013; Alberts et al. 2016; Bufanda et al. 2016). In addition, there are examples where deep *Chandra* observations of $z \sim 1$ quasars are finding hot cluster gas emission (Siemiginowska et al. 2010; Russell et al. 2012; Hlavacek-Larrondo et al. 2016). In fact, Russell et al. (2012) suggests the possibility that high- z cool-core X-ray clusters may be associated with many quasars, but are not-identified due to the glare of the quasar. Lastly, in a study of the AGN emission in BCGs, Hlavacek-Larrondo et al. (2013) finds that these galaxies become significantly more radiatively efficient and luminous at higher redshifts and could host quasars at $z \sim 1$. Taken together, these results all suggest that luminous AGN activity at $z \approx 0.9$ may indeed be common, if not dominant, in $\log(M_h/M_\odot) \gtrsim 14$ haloes. Such a result would be consistent with the major-merger triggering mechanism for AGNs, as these young cluster environments at high redshifts would allow more frequent interactions between gas-rich galaxies than at lower redshift. As the clusters continue to grow and relax, their velocity dispersions increase and interactions become rarer, rapidly reducing the number of luminous AGNs in clusters to the low values observed today (e.g., Ehlert et al. 2015).

If this scenario is accurate, the question arises of why do the previous X-ray clustering analyses all tend to give halo masses of $\log(M_h/M_\odot) \sim 13 - 13.5$ at almost all z . The main difference between the CLF method and more traditional cluster techniques is that the CLF considers the luminosity variation in the clustering, and makes use of the total number density of AGNs at different luminosities and dark matter haloes at different masses as additional constraints. This additional information makes sure that the AGNs are distributed over the range of dark matter halo masses in a way consistent with how r_0 varies with L .

The CLF predictions for the dark matter hosts of quasars is partially based on extrapolations from clustering measurements of lower-luminosity AGNs (e.g., Koutoulidis et al. 2013). Therefore, the additional clustering data of $z \sim 1$ quasars that will be obtained by *eROSITA* will be required to refine the CLF model and explore these predictions in detail.

6 SUMMARY AND CONCLUSIONS

This paper developed a method to constrain the AGN Conditional Luminosity Function (CLF), a luminosity-dependent halo occupation model for AGNs, thereby allowing a connection between AGN properties and its cosmological environment. The method requires the X-ray luminosity function and $r_0(L)$ over a narrow range of redshifts. Using the limited data currently available, a CLF model was constrained at two redshifts, $z \approx 0$ and 0.9 , and the AGN bias, mean halo mass, AGN lifetime, and halo occupation numbers were all calculated as functions of luminosity. Our most important results are:

- The AGN bias and mean halo mass show significant luminosity dependence at both redshifts, specifically for $\log(L/(\text{erg s}^{-1})) \lesssim 44$. This likely indicates a change in AGN fueling processes from low to high luminosity.
- In contrast to earlier clustering analyses, the CLF method predicts that high luminosity AGNs at $z \approx 0.9$ inhabit haloes with $M_h \sim 10^{14} M_\odot$, which are the ancestors of

local massive clusters. This result is consistent with the observed rapid increase with redshift of the luminous AGN fraction within clusters. These environments provide the right setting for strong interactions between the massive gas-rich galaxies needed to fuel luminous nuclear accretion. Additional data from *eROSITA* is needed to further explore this prediction.

- The mean AGN luminosity depends on halo mass at both epochs, but only for $M_h \gtrsim 10^{12} M_\odot$ ($z \approx 0$) or $M_h \gtrsim 10^{13} M_\odot$ ($z \approx 0.9$). We find $L \propto M_h^{0.8}$ at $z \approx 0$ and $L \propto M_h^{1.2}$ at $z \approx 0.9$ indicating that AGNs are spread over a wider mass range for each luminosity at low redshift.
- AGN lifetimes are $\lesssim 10^8$ yrs for all luminosities and redshifts, and are $< 10^6$ yrs for the highest luminosities.
- The CLF-derived results strongly support the idea that at $z \lesssim 1$ AGN triggering evolves from a merger-dominated regime which is only weakly dependent on halo mass to one where the majority of AGNs are triggered by secular processes, including interactions with neighbours (e.g., Koss et al. 2010; Draper & Ballantyne 2012; Hopkins et al. 2014). The high luminosity quasars must still be fueled by a catastrophic interaction with another gas rich galaxy (e.g., Sanders et al. 1988), but such events are rare in the nearby Universe.
- As the CLF method provides a statistical connection between AGN luminosity and host halo masses, it can be used to populate dark matter haloes in cosmological simulations with AGNs of different luminosities in a logical and self-consistent manner.

The CLF method described here relies on the accuracy of the underlying observations. If certain datapoints are biased in some manner (such as the high- L r_0 point at $z \approx 0$; Fig. 1) then the CLF-derived statistics will inherit that bias. However, as observations improve with future observatories and campaigns, the CLF method can quickly incorporate the new data and produce increasingly more accurate predictions. For example, recent work by Mountrichas et al. (2016) indicate that $r_0(L)$ may decrease at $\log L \sim 43.5$ (see also the models of Fanidakis et al. 2013). If this result is confirmed by future observations, the CLF framework can account for it by simply revising the underlying CLF parameterization (Eq. 11). In general, future $r_0(L)$ measurements in the X-ray band will provide the most important improvement to the CLF-derived results.

Future development of the CLF method will occur in two directions. As mentioned earlier, the first direction will focus on including the results from the optical quasar clustering measurements. Additionally, we will also develop a model for the 1-halo term in the AGN correlation function. The 1-halo term dominates at separations $\lesssim 1 \text{ h}^{-1} \text{ Mpc}$ and arises from pairs of AGNs within a single halo (e.g., a central and satellite galaxy). Therefore, it encodes information about AGN triggering on small scales (e.g., mergers and other forms of galaxy harassment). The addition of this term in the method will also allow a connection to more detailed AGN host galaxy properties (e.g., stellar mass) that also depend on position within haloes.

ACKNOWLEDGEMENTS

The author thanks J. Wise, G. Altay, A. Myers, and R. Grissom for help and advice during the course of this work, R. Hickox for comments on a draft of the manuscript, and acknowledges support from NSF award AST 1333360.

REFERENCES

- Aird J., Nandra K., Laird E.S., Georgakakis A., Ashby M.L.N., Barmby P., Coil A.L., Huang J.-S., Koekemoer A.M., Steidel C.C., Willmer C.N.A., 2010, *MNRAS*, 401, 2531
- Aird J., Coil A.L., Georgakakis A., Nandra K., Barro G., Pérez-González P.G., 2015a, *MNRAS*, 451, 1892
- Aird J., et al., 2015b, *ApJ*, 815, 66
- Alberts S., et al., 2016, *ApJ*, in press (arXiv:1604.03564)
- Allevato V., et al., 2011, *ApJ*, 736, 99
- Arnaud K.A., 1996, in Jacoby G., Barnes J., eds, *Astronomical Data Analysis Software and Systems V*, ASP Conf. Ser. Vol. 101, 17
- Ballantyne D.R., 2014, *MNRAS*, 437, 2845
- Ballantyne D.R., 2016, *MNRAS*, submitted (Paper II)
- Baumgartner W.H., Tueller J., Markwardt C.B., Skinner G.K., Barthelmy S., Mushotzky R.F., Evans P.A., Gehrels N., 2013, *ApJS*, 207, 19
- Benson A.J., Frenk C.S., Lacey C.G., Baugh C.M., Cole S., 2002, *MNRAS*, 333, 177
- Bonoli S., Marulli F., Springel V., White S.D.M., Branchini E., Moscardini, L., 2009, *MNRAS*, 396, 423
- Boylan-Kolchin M., Springel V., White S.D.M., Jenkins A., Lemson G., 2009, *MNRAS*, 398, 1150
- Brandt W.N., Alexander D.M., 2015, *A&ARv*, 23, 1
- Brandt, W.N., Hasinger G., 2005, *ARA&A*, 43, 827
- Buchner J., Georgakakis A., Nandra K., Brightman M., Menzel M.-L., Liu Z., Hsu L.-T., Salvato M., Rangel C., Aird J., Merloni A., Ross N., 2015, *ApJ*, 802, 89
- Bufanda E., et al., 2016, *MNRAS*, in press (arXiv:1606.06775)
- Bundy K., et al., 2006, *ApJ*, 561, 120
- Burlon D., Ajello M., Greiner J., Comastri A., Merloni A., Gehrels N., 2011, *ApJ*, 728, 58
- Cappelluti N., Ajello M., Burlon D., Krumpe M., Miyaji T., Bonoli S., Griener, J., 2010, *ApJ*, 716, L209
- Cappelluti N., Allevato V., Finoguenov, A., 2012, *Adv. in Astron.*, 853701
- Carroll S.M., Press W.H., Turner E.L., 1992, *ARA&A*, 30, 499
- Cen R., Safarzadeh M., 2015, *ApJ*, 798, L38
- Chatterjee S., DeGraf C., Richardson J., Zheng Z., Nagai D., Di Matteo T., 2011, *MNRAS*, 419, 2657
- Chatterjee S., Nguyen M.L., Myers A.D., Zheng, Z., 2013, *ApJ*, 779, 147
- Conroy C., Wechsler R.H., Kravtsov A.V., 2006, *ApJ*, 647, 201
- Conroy C., White M., 2013, *ApJ*, 762, 70
- Croom S.M., et al., 2005, *MNRAS*, 356, 415
- Croton D.J. et al., 2006, *MNRAS*, 365, 11
- Croton D.J., 2009, *MNRAS*, 394, 1109
- Davis M., Peebles P.J.E., 1983, *ApJ*, 267, 465
- Della Ceca, R., et al., 2008, *A&A*, 487, 119
- Di Matteo T., Springel V., Hernquist L., 2005, *Nature*, 433, 604
- Draper A.R., Ballantyne D.R., 2011, *ApJ*, 740, 57
- Draper A.R., Ballantyne D.R., 2012, *ApJ*, 751, 72
- Efstathiou G., 1992, *MNRAS*, 256, 43
- Eftekharzadeh, S., et al. 2015, *MNRAS*, 453, 2779
- Ehlert S., Allen S.W., Brandt W.N., Xue Y.Q., Luo B., van der Linden A., Mantz A., Morris R.G., 2013, *MNRAS*, 428, 3509
- Ehlert S., Allen S.W., Brandt W.N., Canning R.E.A., Luo B., Mantz A., Morris R.G., von der Linden A., Xue Y.Q., 2015, *MNRAS*, 446, 2709
- Eisenstein D.J., Hu W., 1998, *ApJ*, 496, 605
- Fanidakis N., et al., 2013, *MNRAS*, 435, 679
- Galametz A., et al., 2009, *ApJ*, 694, 1309
- Georgakakis A., et al., 2009, *MNRAS*, 397, 623
- Georgakakis A., et al., 2015, *MNRAS*, 453, 1946
- Harrison F.A., et al., 2015, *ApJ*, submitted (arXiv:1511.04183)
- Hartwick F.D.A., Schade D., 1990, *ARA&A*, 28, 437
- Hasinger G., Miyaji T., Schmidt M., 2005, *A&A*, 441, 417
- Hernquist L., 1989, *Nature*, 340, 687
- Hickox R.C., et al., 2009, *ApJ*, 696, 891
- Hickox R.C., Mullaney J.R., Alexander D.M., Chen C.-T.J., Civano F.M., Goulding A.D., Hainline K.N., 2014, *ApJ*, 782, 9
- Hinshaw G., et al., 2013, *ApJS*, 208, 19
- Hlavacek-Larrondo J., Fabian A.C., Edge A.C., Ebeling H., Allen S.W., Sanders J.S., Taylor G.B., 2013, *MNRAS*, 431, 1638
- Hlavacek-Larrondo J., Gandhi P., Hogan M.T., Gendron-Marsolais M.-L., Edge A.C., Fabian A.C., Russell H.R., Iwasawa K., Mezuca M., 2016, *MNRAS*, submitted (arXiv:1606.07818)
- Hopkins P.F., Hernquist L., Cox T.J., Di Matteo T., Martini P., Robertson B., Springel V., 2005, *ApJ*, 630, 705
- Hopkins P.F., Hernquist L., Cox T.J., Di Matteo T., Robertson B., Springel V., 2006, *ApJS*, 163, 1
- Hopkins P.F., Hernquist L., Cox T.J., Kereš, D., 2008, *ApJS*, 175, 356
- Hopkins P.F., Kocevski D.D., Bundy K., 2014, *MNRAS*, 445, 823
- Hütsi G., Gilfanov M., Sunyaev R., 2014, *A&A*, 561, A58
- Kauffmann G., Haehnelt M., 2000, *MNRAS*, 311, 576
- Kauffmann G., et al., 2004, *MNRAS*, 353, 713
- Kilbinger M., et al., 2009, *A&A*, 497, 677
- Kolodzig A., Gilfanov M., Sunyaev R., Sazonov S., Brusa, M., 2013, *A&A*, 558, A89
- Kolodzig A., Gilfanov M., Hütsi G., Sunyaev, R., 2013, *A&A*, 558, A90
- Koss M., Mushotzky R., Veilleux S., Winter L., 2010, *ApJ*, 716, L125
- Koutoulidis L., Plionis M., Georgantopoulos I., Fanidakis, N., 2013, *MNRAS*, 428, 1382
- Krumpe M., Miyaji T., Husemann B., Fanidakis N., Coil A.L., Aceves H., 2015, *ApJ*, 815, 21
- La Franca F., et al., 2005, *ApJ*, 635, 864
- Leauthaud A., et al., 2015, *MNRAS*, 446, 1874
- Lidz A., Hopkins P.F., Cox T.J., Hernquist L., Robertson, B., 2006, *ApJ*, 641, 41
- Martini P., 2004, in Ho L.C., ed., *Coevolution of Black Holes and Galaxies*. Cambridge University Press, Cambridge, p. 169
- Martini P., Weinberg D.H., 2001, *ApJ*, 547, 12
- Martini P., et al., 2013, *ApJ*, 768, 1
- Menci N., Fontana A., Giallongo E., Grazian A., Salimbeni S., 2006, *ApJ*, 647, 753
- Mendez, A.J. et al., 2016, *ApJ*, 821, 55
- Merloni A., Heinz S., 2013, in Oswald T.D., Keel W.C., eds., *Planets, Stars and Stellar Systems Vol. 6*. Springer Science+Business Media, Dordrecht, p. 503
- Metropolis N., Rosenbluth A.W., Rosenbluth M.N., Teller A.H., Teller, E., 1953, *J. Chem. Phys.*, 21, 1087
- Miyaji T., Krumpe M., Coil A.L., Aceves H., 2011, *ApJ*, 726, 83
- Moran E.C., Filippenko A.V., Chornock R., 2002, *ApJ*, 579, L71
- Mountrichas G., Georgakakis A., Menzel M.-L., Fanidakis N., Merloni A., Liu Z., Salvato M., Nandra K., 2016, *MNRAS*, 457, 4195
- Myers A.D., Brunner R.J., Nichol R.C., Richards G.T., Schneider D.P., Bahcall N.A., 2007, *ApJ*, 658, 85
- Nandra K., O’Neill P.M., George I.M., Reeves J.N., 2007, *MNRAS*, 382, 194
- Navarro J.F., Frenk C.S., White S.D.M., 1997, *ApJ*, 490, 493

- Nickerson S., Stinson G., Couchman H.M.P., Bailin J., Wadsley J., 2011, MNRAS, 415, 257
- Peebles P.J.E., 1980, The Large Scale Structure of the Universe, (Princeton, NJ: Princeton Univ. Press)
- Popesso P., Biviano A., 2006, A&A, 460, L23
- Porciani C., Magliocchetti M., Norberg, P., 2004, MNRAS, 355, 1010
- Richardson J., Zheng Z., Chatterjee S., Nagai D., Shen Y., 2012, ApJ, 755, 30
- Richardson J., Chatterjee S., Zheng Z., Myers A.D., Hickox R., 2013, ApJ, 774, 143
- Ross N.P., et al., 2009, ApJ, 697, 1634
- Russell H.R., Fabian A.C., Taylor G.B., Sanders J.S., Blundell K.M., Crawford C.S., Johnstone R.M., Belsole E., 2012, MNRAS, 422, 590
- Salucci P., Szuszkiewicz E., Monaco P., Danese L., 1999, MNRAS, 307, 637
- Sanders D.B., Soifer B.T., Elias J.H., Madore B.F., Matthews K., Neugebauer G., Scoville N.Z., 1988, ApJ, 325, 74
- Scoccimarro R., Sheth R.K., Hui L., Jain B., 2001, ApJ, 546, 20
- Shen Y., 2009, ApJ, 704, 89
- Shen Y., et al. 2013, ApJ, 778, 98
- Shen S., Madau P., Conroy C., Governato F., Mayer L., 2014, ApJ, 792, 99
- Siemiginowska A., Burke D.J., Aldcroft T.L., Worrall D.M., Allen S., Bechtold J., Clarke T., Cheung C.C., 2010, ApJ, 722, 102
- Sijacki D., Vogelsberger M., Genel S., Springel V., Torrey P., Snyder G.F., Nelson D., Hernquist L., 2015, MNRAS, 452, 575
- Smith R.E., et al., 2003, MNRAS, 341, 1311
- Springel V., et al., 2005, Nature, 435, 629
- Springel V., Di Matteo T., Hernquist L., 2005, MNRAS, 361, 776
- Tinker J.L., Robertson B.E., Kravtsov A.V., Klypin A., Warren M.S., Yepes G., Gottlöber S., 2010, ApJ, 724, 878
- Triester E., Urry C.M., 2012, Adv. in Astron., 516193
- Trump J.R., et al., ApJ, 811, 26
- Ueda Y., Akiyama M., Ohta K., Miyaji, T., 2003, ApJ, 598, 886
- Ueda Y., Akiyama M., Hasinger G., Miyaji T., Watson M.G., 2014, ApJ, 786, 104
- van den Bosch F.C., 2002, MNRAS, 331, 98
- van den Bosch F.C., Yang X., Mo H.J., 2003, MNRAS, 340, 771
- van den Bosch F., et al., 2007, MNRAS, 376, 841
- Vasudevan R.V., Fabian A.C., 2009, MNRAS, 392, 1124
- Yang X., Mo H.J., van den Bosch, F., 2003, MNRAS, 339, 1057
- Zehavi, I., et al. 2011, ApJ, 736, 59
- Zheng Z., Coil A.L., Zehavi I., 2007, ApJ, 667, 760

APPENDIX A: DETAILS ON THE COSMOLOGICAL CALCULATIONS

First, define a dark matter halo of mass M_h as

$$M_h = \frac{4}{3} \pi R_h^3 \bar{\rho}_m(z) \Delta, \quad (\text{A1})$$

where R_h is the radius of the halo, and $\Delta = 200$ quantifies the overdensity of the halo compared to the average density of the Universe; i.e., $\Delta \bar{\rho}_m = \Delta \rho_{\text{crit}} \Omega_m(z)$ (ρ_{crit} is the critical density).

With M_h now specified, the fitting formulas computed by Tinker et al. (2010) are used to compute $n(M_h)$ and $b(M_h)$ at the required redshifts. In order to use these formulas, the smoothed variance of the linear density field is needed:

$$\sigma^2(r) = \frac{1}{2\pi^2} \int P(k) \hat{W}^2(kr), \quad (\text{A2})$$

where

$$P(k, z) = P_i(k) T^2(k) D^2(z) \quad (\text{A3})$$

is the linear power spectrum and

$$\hat{W}(kr) = \frac{3}{(kr)^3} (\sin(kr) - kr \cos(kr)) \quad (\text{A4})$$

is the Fourier transform of the top-hat window function in real space. The shape of the power spectrum of fluctuations is initially assumed to be $P_i \propto k$ and then is modified using the transfer function $T(k)$ fitting formula provided by Eisenstein & Hu (1998) and the growth function $D(z)$ (Carroll, Press & Turner 1992). The normalization of $P(k)$ is set by using the local value of σ for spheres of radius $8 h^{-1} \text{Mpc}$, σ_8 .

The calculation of ξ_{dm}^{2h} requires computing both the ‘1-halo’ and total dark matter correlation functions. The latter is computed from the non-linear evolved power spectrum $P_{\text{NL}}(k)$ via a Fourier Transform,

$$\xi_{\text{dm}}(r) = \frac{1}{2\pi^2} \int_0^\infty k^3 P_{\text{NL}}(k) \frac{\sin kr}{kr} \frac{dk}{k}. \quad (\text{A5})$$

The NICEA code (Kilbinger et al. 2009) is used to calculate P_{NL} at the needed z using the Smith et al. (2003) fitting function and the Eisenstein & Hu (1998) transfer function. The resulting $\xi_{\text{dm}}(r)$ closely follow the results from the Millennium II simulation (Boylan-Kolchin et al. 2009) at radii $r \gtrsim 1 h^{-1} \text{Mpc}$ (after correcting for the difference in σ_8).

The ‘1-halo’ term of the correlation function is (van den Bosch et al. 2003)

$$\xi_{\text{dm}}^{1h}(r) = \int_0^\infty dk k^2 \frac{\sin kr}{kr} \int_0^\infty dM_h n(M_h) |\hat{\delta}(M_h, k)|^2, \quad (\text{A6})$$

where $\hat{\delta}(M_h, k)$ is the Fourier Transform of the halo density profile truncated at the virial radius. Here, a Navarro-Frenk-White (NFW; Navarro, Frenk & White 1997) density profile is assumed for the halo and the formulas for computing $\hat{\delta}(M_h, k)$ are given by Scoccimarro et al. (2001). The evolution of the halo concentration parameter with z and M_h is calculated using the relation of Zheng, Coil & Zehavi (2007). The ‘2-halo’ term is then computed from $\xi_{\text{dm}}^{2h}(r) = \xi_{\text{dm}}(r) - \xi_{\text{dm}}^{1h}(r)$ assuming that $\xi_{\text{dm}}(r) = \xi_{\text{dm}}^{1h}(r)$ at $r = 0.01 \text{Mpc}$.

APPENDIX B: LIGHT-CONE EFFECTS ON THE CLF

In a situation where the data constraining the AGN CLF is accumulated over a significant redshift range than a more accurate CLF might be determined by averaging $n(M_h)$ and $\xi_{\text{dm}}^{2h}(r)$ over z . For example, if the AGN data is gathered between z_{min} and z_{max} , then the XLF would be

$$\phi(L) = \int_0^\infty \Psi(L|M_h) n_{\text{eff}}(M_h) dM_h, \quad (\text{B1})$$

where

$$n_{\text{eff}}(M_h) = \frac{1}{V} \int_{z_{\text{min}}}^{z_{\text{max}}} \frac{dV}{dz} n(M_{\text{eff}}, z) dz \quad (\text{B2})$$

and

$$V = \int_{z_{\text{min}}}^{z_{\text{max}}} \frac{dV}{dz} dz. \quad (\text{B3})$$

Similarly, the AGN correlation function is now

$$\xi_{\text{AA}}^{2h}(r) \approx \bar{b}_A^2 \xi_{\text{dm,eff}}^{2h}(r), \quad (\text{B4})$$

where

$$\xi_{\text{dm,eff}}^{2h}(r) = \frac{\int_{z_{\text{min}}}^{z_{\text{max}}} \frac{dV}{dz} n^2(M_h, z) \xi_{\text{dm}}^{2h} dz}{\int_{z_{\text{min}}}^{z_{\text{max}}} \frac{dV}{dz} n^2(M_h, z) dz} \quad (\text{B5})$$

and

$$\bar{b}_A = \frac{1}{\phi(L)} \int_0^\infty \Psi(L|M_h) b_h(M_h) n_{\text{eff}}(M_h) dM_h. \quad (\text{B6})$$

In these equations, dV/dz is the comoving volume element per unit solid angle.

This paper has been typeset from a $\text{T}_{\text{E}}\text{X}/\text{L}^{\text{A}}\text{T}_{\text{E}}\text{X}$ file prepared by the author.